Zhao *et al.*
Chinese Journal of Mechanical Engineering (2023) 36:97
https://doi.org/10.1186/s10033-023-00927-0

Chinese Journal of Mechanical Engineering

ORIGINAL ARTICLE

Open Access

Nanometric Cutting Mechanism of Cerium–Lanthanum Alloy

Chenyu Zhao[1], Min Lai[1*] and Fengzhou Fang[1,2]

Abstract

Cerium–lanthanum alloy is widely used in the green energy industry, and the nanoscale smooth surface of this material is in demand. Nanometric cutting is an effective approach to achieving the ultra-precision machining surface. Molecular dynamics (MD) simulation is usually used to reveal the atomic-scale details of the material removal mechanism in nanometric cutting. In this study, the effects of cutting speed and undeformed chip thickness (UCT) on cutting force and subsurface deformation of the cerium–lanthanum alloy during nanometric cutting are analyzed through MD simulation. The results illustrate that the dislocations, stacking faults, and phase transitions occur in the subsurface during cutting. The dislocations are mainly Shockley partial dislocation, and the increase of temperature and pressure during the cutting process leads to the phase transformation of γ-Ce (FCC) into β-Ce (HCP) and δ-Ce (BCC). β-Ce is mainly distributed in the stacking fault area, while δ-Ce is distributed in the boundary area between the dislocation atoms and γ-Ce atoms. The cutting speed and UCT affect the distribution of subsurface damage. A thicker deformed layer including dislocations, stacking faults and phase-transformation atoms on the machined surface is generated with the increase in the cutting speed and UCT. Simultaneously, the cutting speed and UCT significantly affect the cutting force, material removal rate, and generated subsurface state. The fluctuations in the cutting force are related to the generation and disappearance of dislocations. This research first studied the nanometric cutting mechanism of the cerium–lanthanum ally, providing a theoretical basis for the development of ultra-precision machining techniques of these materials.

Keywords Cerium–lanthanum alloy, Molecular dynamics simulation, Nanometric cutting, Subsurface damage

1 Introduction

Metallic cerium is a complicated metal with multiple allotropic forms such as α-Ce, β-Ce, γ-Ce and δ-Ce [1]. Each form has a distinct structure and is stable with specific temperature and pressure conditions [2]. Metallic lanthanum and metallic cerium can form a cerium–lanthanum alloy with any proportion, which plays an important role in the green energy industry [3, 4]. However, cerium–lanthanum alloy is prone to oxidation, which brings great difficulties to the application. Thus, improving the corrosion resistance of this material is of great significance. Good surface quality, characterized by nanoscale surface roughness, can significantly improve the corrosion resistance of these materials. Currently, the common way to obtain nanoscale surface roughness of cerium–lanthanum alloy is single-point diamond turning (SPDT), where the undeformed chip thickness (UCT) could be as small as nanoscale and the material characteristics have an important effect on the deformation process of the material. Therefore, it is significant to study the nanometric cutting mechanism of the cerium–lanthanum alloy.

Whereas, under the current SPDT experiment conditions, it is time-consuming and difficult to conduct stable

*Correspondence:
Min Lai
laimin@tju.edu.cn
[1] State Key Laboratory of Precision Measuring Technology & Instruments, Laboratory of Micro/Nano Manufacturing Technology (MNMT), Tianjin University, Tianjin 300072, China
[2] Centre of Micro/Nano Manufacturing Technology (MNMT-Dublin), University College Dublin, Dublin 4, Ireland

cutting experiments at the nanometer scale and perform effective cutting process analysis, such as material processing damage and deformation process, cutting force, and cutting heat [5]. However, performing a molecular dynamics (MD) simulation is convenient to understand the processing mechanism at the atomic and close-to-atomic scale, where the motion trail of material atoms is simulated so that the atomic structure and physical properties of the entire system can be determined. Fang [6] pointed out the importance of atomic and close-to-atomic scale manufacturing (ACSM) to the development of future technologies and high-end component manufacturing. The typical characteristic of ACSM is that energy directly affects the atom to be removed, migrated and added, which requires powerful computing power [7]. The emergence of supercomputing promotes greatly the progress of computational materials science, and MD simulation has become an important method to analyze the microscopic mechanism of materials.

In recent years, MD simulation was widely used to analyze the nanometric cutting mechanism of various materials, since it can simulate the cutting process with relatively complex movement and analyze the distribution of material subsurface damage in a large range. For examples, the crystal orientation effect on the subsurface deformation of monocrystalline germanium in nanometric cutting was studied by MD simulation [8]. Pei et al. [9] simulated the nanometric cutting process of metallic copper using EAM potential function and studied the influence of machining parameters on the formation of surface morphology and subsurface defects in the workpiece. Fan et al. [10] simulated the changes of physical quantities such as cutting temperature, cutting force and coordination number of single crystal gallium arsenide in nanometric cutting, and found that the anisotropy of gallium arsenide would affect the cutting performance greatly. As for cerium and lanthanum, Zhang et al. [11] used MD simulation to study the influence of cutting parameters on the surface quality of metallic cerium. Di Wu et al. [12] derived the potential function of the isomorphic phase transition of metallic cerium and fitted the relevant parameters, followed by its verification through MD simulation. Fu et al. [13] established a specific form of the potential function (EAM) for metallic cerium and metallic lanthanum. The simulation results were in good agreement with the experimental data.

Whereas, so far, there has been no analysis of the MD simulation of the cerium–lanthanum alloy. Compared with metallic cerium, the cerium–lanthanum alloy is more prone to oxidation reactions in actual machining [14]. It is necessary to study the mechanism of its microscopic deformation and understand the law of its deformation. Consequently, based on the different parameters of cutting (including cutting speed and UCT), this study established a series of simulation models for cutting the cerium–lanthanum alloy using diamond tools. The cutting force, phase transition of the subsurface, and formation and distribution of the damage during the cutting process of the cerium–lanthanum alloy were studied in depth.

2 Models and Potential Function

The Large Atomic/Molecular Massively Parallel Simulator (LAMMPS) was used for cutting simulation. The model comprises a diamond tool and the workpiece of the cerium–lanthanum alloy, as shown in Figure 1. The machined surface is (0 0 1) plane, and the diamond tool moves along $[\bar{1}\,0\,0]$ orientation. The size of the workpiece was set to 40 nm × 25 nm × 20 nm, and the diamond tool had an edge radius of 10 nm. Fixed boundary conditions were applied in the *X*, *Y*, and *Z* directions. The atoms in the workpiece of the cerium–lanthanum alloy were divided into boundary atoms, thermostatic atoms, and Newtonian atoms. The boundary atoms keep the material fixed during the cutting process of the diamond tool. The thermostatic atoms remain at a constant temperature of 300 K, which ensures the heat dissipation of materials in the nanometric cutting process. The Newtonian atoms simulate the motion of atoms in the real process of cutting. Since the force between the carbon atoms inside the diamond tool is not considered, the diamond tool is regarded as a rigid body.

In 2013, Fu et al. [13] developed the potential function of Gupta type (EAM); successfully gave the specific expression of the multi-body potential function, which described the interaction of Ce–Ce, Ce–La, and La–La; and fitted the unknown parameters in this potential function, which was verified by LAMMPS and was in good agreement with the data measured in the actual experiment. The formula of the potential function is expressed

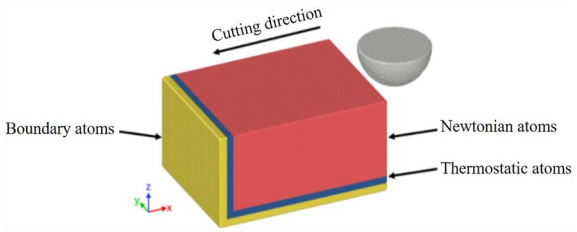

Figure 1 3D Simulation model

Table 1 Gupta potential function parameters

	U (eV)	*A*	*p*	*q*	r_0 (nm)
La	1.346859	0.113505	11.37958	0.545680	0.3755
Ce	0.914951	0.069013	14.23911	0.271883	0.3649

Table 2 L-J potential function parameters

	C—Ce	C—La
ϵ	0.0016021	0.0018321
σ	3.2994	3.2843

Table 3 Parameters of MD model

Condition	Parameter
Work material	Ce-5La alloy
Lattice constant	A = 0.516 nm
Tool edge radius	10 nm
Cutting direction	[$\bar{1}$ 0 0] on the (0 0 1) plane
Initial bulk temperature	298 K
Workpiece dimensions	40 nm × 25 nm × 20 nm

in Eq. (1), and the parameters of the potential function are listed in Table 1 [13].

$$E_C = \frac{U}{2}\sum_i \left(\sum_{j(\neq i)} A\exp\left(-p\left(\frac{r_{ij}}{r_0}-1\right)\right) - \left(\sum_{j(\neq i)} \exp\left(\left(-2q\left(\frac{r_{ij}}{r_0}-1\right)\right)\right)\right)^{\frac{1}{2}} \right), \tag{1}$$

where E_c is the cohesive energy per atom in a solid; U, A, p, q are empirical parameters; r_0 is the equilibrium first-neighbor distance; r_{ij} represents the distance between atom i and atom j. The cutoff distance for the potential is set as large as 1.2 nm.

In previous studies, the interaction between the tool and workpiece was described by the pair potential function [15, 16]. Therefore, the interaction potential between C-Ce and C-La chosen in this study is L-J potential function. The specific formula of the potential function of L-J is illuminated in Eq. (2) [17]. Table 2 lists the parameters of the potential function between different atom pairs.

$$y = 4\varepsilon\left[\left(\frac{\sigma}{r_{ij}}\right)^{12} - \left(\frac{\sigma}{r_{ij}}\right)^{6}\right], \tag{2}$$

where y is the Lennard-Jones term; ε is the depth of the potential well, and σ is the (finite) distance at which the interparticle potential is zero; r_{ij} represents the distance between atom i and atom j.

Table 4 Cutting speed and UCT in each model

	Model 1	Model 2	Model 3	Model 4	Model 5
UCT (nm)	2	4	6	4	4
Cutting speed (m/s)	500	500	500	100	300

Table 3 presents the other simulation details, and Table 4 presents the parameters of the nanometric cutting simulation. The cerium–lanthanum alloy was modeled by random substitution, replacing 5% atoms in the model of the atoms of cerium with the atoms of lanthanum at random. The Open Visualization Tool (OVITO) software was used to visualize the data of MD [18]. Both metallic cerium and metallic lanthanum are FCC structures, and the data analysis can be performed directly through OVITO.

3 Result and Analysis

3.1 Cutting Force and Evolution of Subsurface Damage

The cutting force is an important factor that associates cutting energy and tool wear [19]. Taking Model 2 as an example, the cutting speed is 500 m/s and the UCT is 4 nm. Figure 2 confirms the variation in the cutting force and the formation and distribution of dislocation damage and lattice defects on the subsurface at the corresponding position of the workpiece. The analysis of common neighbour analysis (CNA) can obtain the phase transition and lattice defects of the workpiece. The dislocation analysis (DXA) can acquire the type and distribution of dislocation lines inside the workpiece.

In the initial stages of cutting, both the tangential and normal forces increase gradually, and as the cutting progresses, they no longer increase significantly but fluctuate at 60 nN and 100 nN, respectively, until the simulation ends. The normal force is greater in the simulation process because the negative rake angle of the cutting is large when the UCT is small; thus, the normal force dominates the resistance of the material [20]. Nonetheless, there are large fluctuations in the cutting force during the cutting process. In the previous study on nanoindentation of metallic copper, the fluctuation of indentation force is explained as the continuous nucleation of dislocations

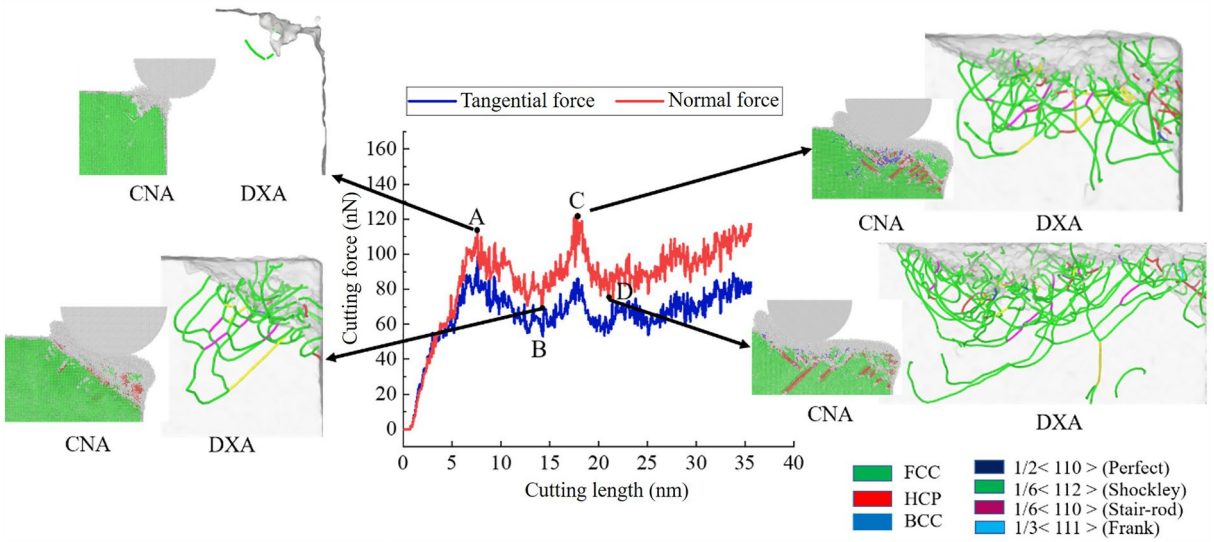

Figure 2 The cutting force and the distribution of subsurface dislocation and lattice structural change when the cutting speed is 500 m/s and the UCT is 4 nm.

[21]. In this study, the relationship between cutting force fluctuates (points *A*, *B*, *C*, *D* in Figure 2) and dislocation formation in cerium–lanthanum alloy during nanometric cutting is analyzed. The atoms of the FCC, HCP, and BCC structures are indicated in green, red, and blue, respectively, in the lattice defect analysis. The green dislocation line is the Shockley partial dislocation, and the blue dislocation line is the Frank partial dislocation in the dislocation analysis.

When the diamond tool cuts the workpiece, the atoms in the front of the rake face produce shear slip due to the extrusion and shearing action of the tool, which forms a zone of shear slip. A part of the atoms in the slip zone moves upward along the rake face, which forms the chip. And other atoms in the slip zone slide down and form a rough machined surface under the action of the squeezing friction of the flank surface. As the tool moves forward, the atoms at the chip accumulate so that both the tangential and normal forces continue to increase. At point *A* (see Figure 2), some of the workpiece atoms migrate in the cutting process and gradually form lattice defects, which include the Shockley partial dislocation and stacking faults. Perfect dislocation splits in Shockley partial dislocation in the FCC structure. This action is accompanied by a reduction in the elastic energy, which is balanced by the energy of the stacking fault between the part of the dislocations. Consequently, the formation of dislocations leads to the release of the accumulated cutting energy, resulting in a temporary reduction in the cutting force, i.e., the cutting force after point *A* is significantly reduced. As the cutting progresses, the cutting tool continues to squeeze and rub the surface atoms of cerium–lanthanum alloy, and the energy of the surrounding atoms gradually accumulates into high-energy atoms. These high-energy atoms are released when the energy they carry exceeds a certain threshold, forming dislocations on the subsurface, and the friction leads to the formation of a large number of dislocations. Dislocations continue to nucleate, multiply, and move. At the same time, due to the pushing action of the tool, a large number of dislocations are generated in front of and below the tool on the subsurface. The intersection of dislocation and dislocation jog occurs on the subsurface of the workpiece. As time progresses, this can lead to a dislocation pile-up, which results in high-stress concentration and improved strength of the workpiece. At the same time, the dislocation pile-up hinders the dislocation slip, and the plastic deformation of the cerium–lanthanum alloy is inhibited. To overcome the dislocation pile-up, a greater external force is required. At this time, the cutting force gradually increases, and energy accumulates at the position of the dislocation pile-up. When the threshold is exceeded, the dislocation climb occurs at this moment according to the lattice defect and dislocation analyses, as shown at point *B* in Figure 2. The Frank partial dislocation is generated inside the workpiece for the first time at this moment. The direction of the dislocation slip is <1 1 1>. The generation of Frank partial dislocation means that the dislocation climb occurs inside the workpiece at this time, which confirms the previous analysis. Frank partial dislocation climbs the zone of the dislocation pile-up and continues to move forward; soon afterward, the energy is released and stress is gradually relaxed. The dislocation slips gradually and spreads to the

depth of the workpiece and finally annihilates on the free surface and the interior of the workpiece. Consequently, under the extrusion and shearing action of the tool, the atoms in the shear zone have a large displacement and generate a dislocation source. As the tool moves forward, a new dislocation source is generated; accordingly, the periodic movement corresponds to the change in the cutting force.

In summary, the cerium–lanthanum alloy generates a large number of dislocations during nanometric cutting. The generation of dislocations and the occurrence of the dislocation pile-up in the workpiece lead to an evident fluctuation in the cutting force.

From Figure 2, it can be seen that there is a change in the lattice structure inside the workpiece during the nanometric cutting according to the analysis of CNA; the original perfect FCC lattice structure is destroyed, and more stacking faults occur on the subsurface [22]. In FCC crystals, the stacking fault is a thin layer comprising an HCP crystal structure. Analogously, there is Shockley partial dislocation at the junction of the stacking fault and the FCC structure of the workpiece. As the cutting progresses, some of the stacking faults move to the internal area of the workpiece, leaving a number of stable subsurface damages. And some of the stacking faults move to the free surface and disappear naturally. It can be seen that when the cutting force reaches the maximum value at point *C* (see Figure 2) according to the analysis of CNA, a large number of FCC lattice structures are transformed into BCC lattice structures, and more BCC lattice structures are found on the subsurface of the workpiece.

There are many mechanisms of dislocation multiplication: Frank-Read source, the mechanism of double-cross slip, the mechanism of climbing and dislocations nucleated at the cutting surface [23]. According to the analysis of CNA, it can be found that with the movement of the tool at point *D* (see Figure 2), the stacking fault gradually moves, and the internal stress is released. The BCC lattice structure then gradually changes to the FCC lattice structure at this moment. The subsurface is mainly composed of stacking faults, which comprise an HCP lattice structure. It can be analyzed that a large number of dislocations, mainly Shockley partial dislocations, are generated during the stable cutting process at points *C* and *D* (see Figure 2). The stack faults nucleated and extended under the cutter, and annihilated on the free surfaces and inside the workpiece. Eventually, dislocation lines form on the surface. At the same time, Shockley partial dislocations slip inside the material and interact with the dislocations under the tool.

The Metallic cerium is prone to phase transition when the external temperature or pressure changes. It mostly exists as γ-Ce (FCC) under normal temperature and pressure. Nevertheless, γ-Ce will transform gradually into β-Ce (HCP) as the pressure increases. And γ-Ce will transform gradually into δ-Ce (BCC) under high temperatures (about 1041 K) and high pressure. Accordingly, there are many phase transitions in nanometric cutting, which is in good agreement with actual metallic cerium.

As shown in Figure 2, the contact area between the tool and workpiece gradually increases as the tool moves during the machining and the pressure increases. The surface temperature of the workpiece does not reach the phase-transition temperature of δ-Ce because of the short cutting time at the initial stage; and δ-Ce of the BCC structure is not produced. As the cutting progresses, the friction between the tool atoms and workpiece atoms intensifies. This results in increased pressure and temperature at the machining area, where the γ-Ce atoms gradually transform into β-Ce and δ-Ce atoms. As shown in Figure 2, the effect of temperature on the depth of the workpiece decreases as the tool cuts steadily. There is a phase transition from γ-Ce to δ-Ce only in the contact area between the tool and the workpiece.

Figure 3 demonstrates the number of atoms in the subsurface phase transition at different cutting lengths. It can be found that as the cutting progresses, the phase transitions of the atoms of metallic cerium increase. At the beginning of cutting, a similar number of γ-Ce atoms are transformed into δ-Ce and β-Ce atoms, but as the cutting progresses, an increasing number of γ-Ce atoms are transformed into β-Ce atoms. When the cutting is stable, there are more β-Ce atoms inside the workpiece. This is because the condition of β-Ce phase-transition is relatively easy as only a certain high pressure is required. Nevertheless, the conditions for the δ-Ce phase transition are more stringent, requiring high temperature and pressure; Consequently, the number of δ-Ce atoms is relatively low.

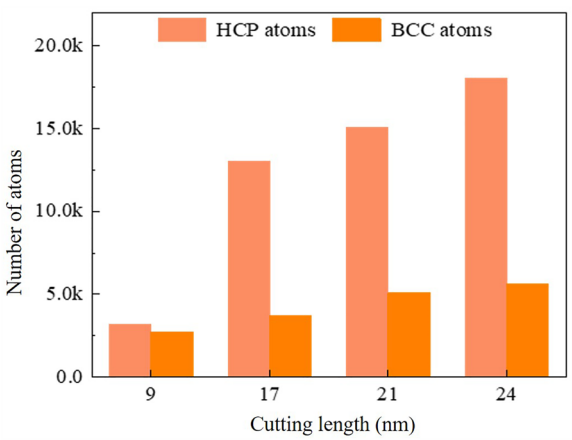

Figure 3 Total number of phase-transition atoms of metallic cerium

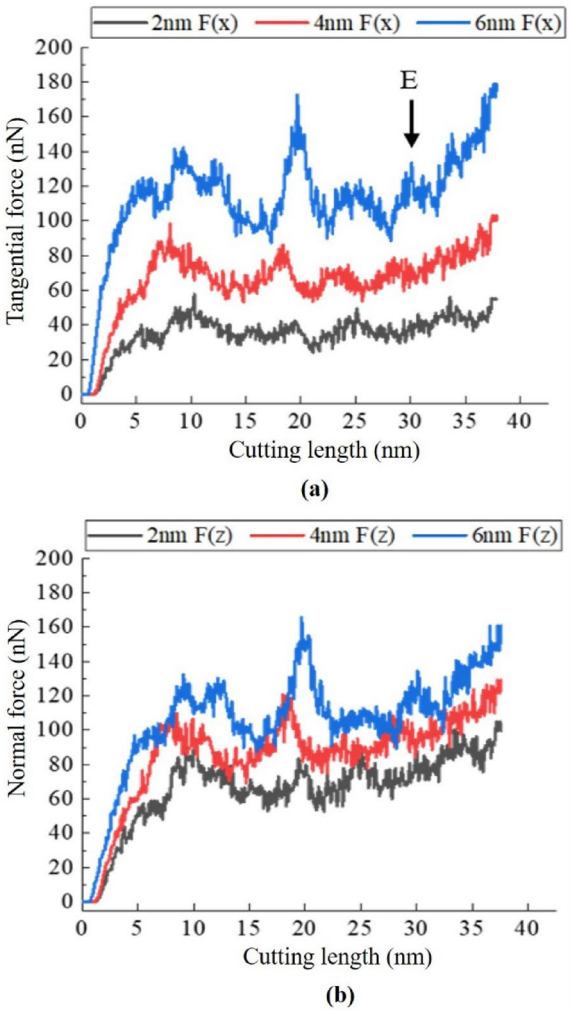

Figure 4 Cutting forces for different models (cutting speed = 500 m/s, UCT = 2 nm, 4 nm, 6 nm): (**a**) Comparison of tangential force of different models, (**b**) Comparison of normal force of different models

3.2 Influence of Machining Parameters on Subsurface Damage

3.2.1 Influence of UCT

As shown in Figure 4, the tangential force F_x and the normal force F_z in each model increase rapidly in the initial stage of the cutting. F_z is greater than F_x, in all models except Model 3, due to the larger negative rake angle. The greater the UCT, the smaller the difference between F_x and F_z. This is because when the UCT is larger, more atoms move upward from the stagnant area to chips, which requires a greater tangential force to push the chip forward. Consequently, when the UCT is relatively large, such as 6 nm, the growth rate in the tangential force is evidently equal to that in the normal force. And the greater the depth of the cutting, the greater the normal force and the growth rate of the normal force in the initial stage.

In addition, when the cutting length is 20 nm according to Figure 4, the cutting forces of the three models produce large fluctuations at the same time. Point E, which has a steady cut, is selected to analyze the lattice defects of the three models, as shown in Figure 4.

Figure 5 confirms the formation and distribution of subsurface damage corresponding to different UCTes of point E (see Figure 4). The greater the UCT, the deeper the depth of the stacking fault and the wider the range of influence. Lattice defects are only concentrated in the machining area for Model 1(UCT = 2 nm), and there are fewer phase-transition atoms. Dislocations and stacking faults move to the free surface and boundary. Most of the defects disappear with the release of stress, and only a small part of the defects remains on the subsurface, which has been cut. As the UCT increases, lattice defects, such as dislocation, remain on the machined surface, and significant stacking faults occur on the subsurface of the machined area in front of the tool. When the UCT is 4 nm, dislocations are concentrated mainly in the machined area, and there is an evident area of dislocation pile-up on the processed surface, which will cause concentrated residual stress. When the UCT is 6 nm, the δ-Ce is almost concentrated on the contact surface between the tool and the workpiece. When the UCT is greater, there is more friction between the atoms, which leads to higher temperatures and phase transitions.

Figure 6(a) and (b) shows that when the UCT is greater, the number of phase-transition atoms is more and the length of the subsurface dislocation is longer. This also proves that when the UCT increases, the subsurface defect is more likely to remain on the machined surface. When the number of dislocations is more on the subsurface, the dislocation length is longer, which is more likely to cause the phenomenon of dislocation pile-up. This leads to local stress concentration and eventually intensifies plastic deformation. Figure 6(c) illustrates that when the UCT increases, the number of Shockley partial dislocations and Frank partial dislocations are more on the subsurface, and the plastic deformation intensifies. Shockley partial dislocations are distributed at the interface between the intact crystal and stacking fault. When the length of Shockley partial dislocations is higher, and the number of dislocation segments is more, the number of generated stacking faults is more. Shockley partial dislocation slips on the slip plane and makes the stacking faults gradually expand. When the UCT is 2 nm, the number of Frank partial dislocations is zero. At this moment, the dislocation can only slip on the dislocation surface, and the generation of dislocation is less, and

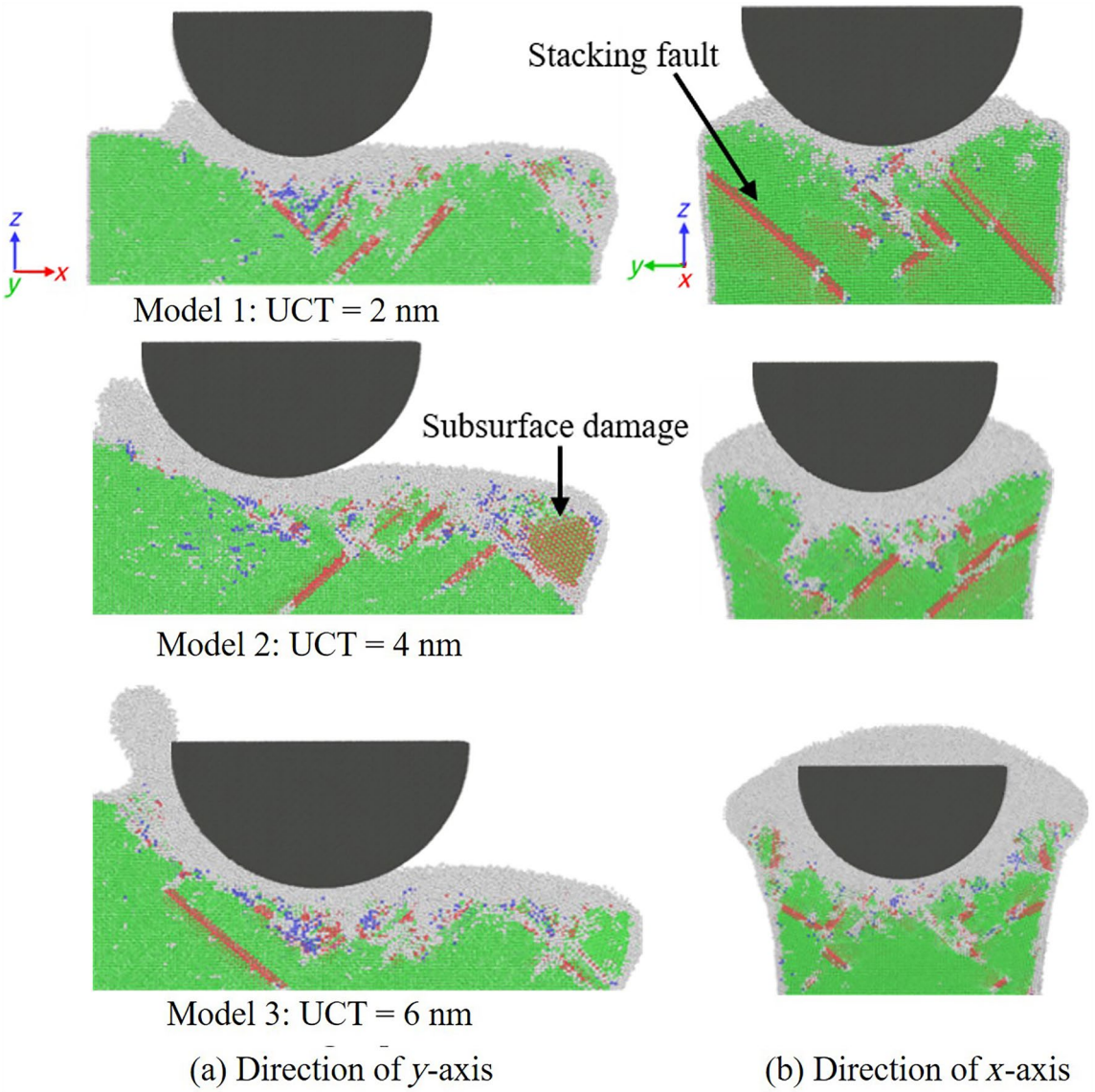

Figure 5 Analysis of subsurface lattice defects for different models: Model 1-3 respectively represent the cutting speed = 500 m/s, and the UCT = 2 nm, 4 nm, 6 nm: (**a**) Direction of *y*-axis, (**b**) Direction of *x*-axis

the phenomenon of dislocation pile-up will not appear. When the UCT is 6 nm, a large number of Frank partial dislocations are generated. This proves that the movement of dislocations occurs at this time. The dislocations climb along the surface of the stacking fault through the movement of the point defect, which makes the surface of the stacking fault enlarge.

In summary, different UCTs correspond to different mechanisms of plastic deformation. When the UCT is small, only Shockley partial dislocation slip occurs on the {1 1 1} plane homogeneously. When the UCT increases, the mechanism of plastic deformation is the common effect of the slippage of Shockley partial dislocation and the climbing of Frank partial dislocation for the cerium–lanthanum alloy.

3.2.2 Influence of Cutting Speed

As shown in Figure 7, when the cutting speed is higher, the location of the formation of the stacking faults is shallow inside the workpiece. The dislocations nucleate on the cutting surface and multiply further into the workpiece. The higher the cutting speed, the fewer dislocations and stacking faults are left after the release of stress in the processed area. When the cutting speed reaches 500 m/s, the dislocations and stacking faults are

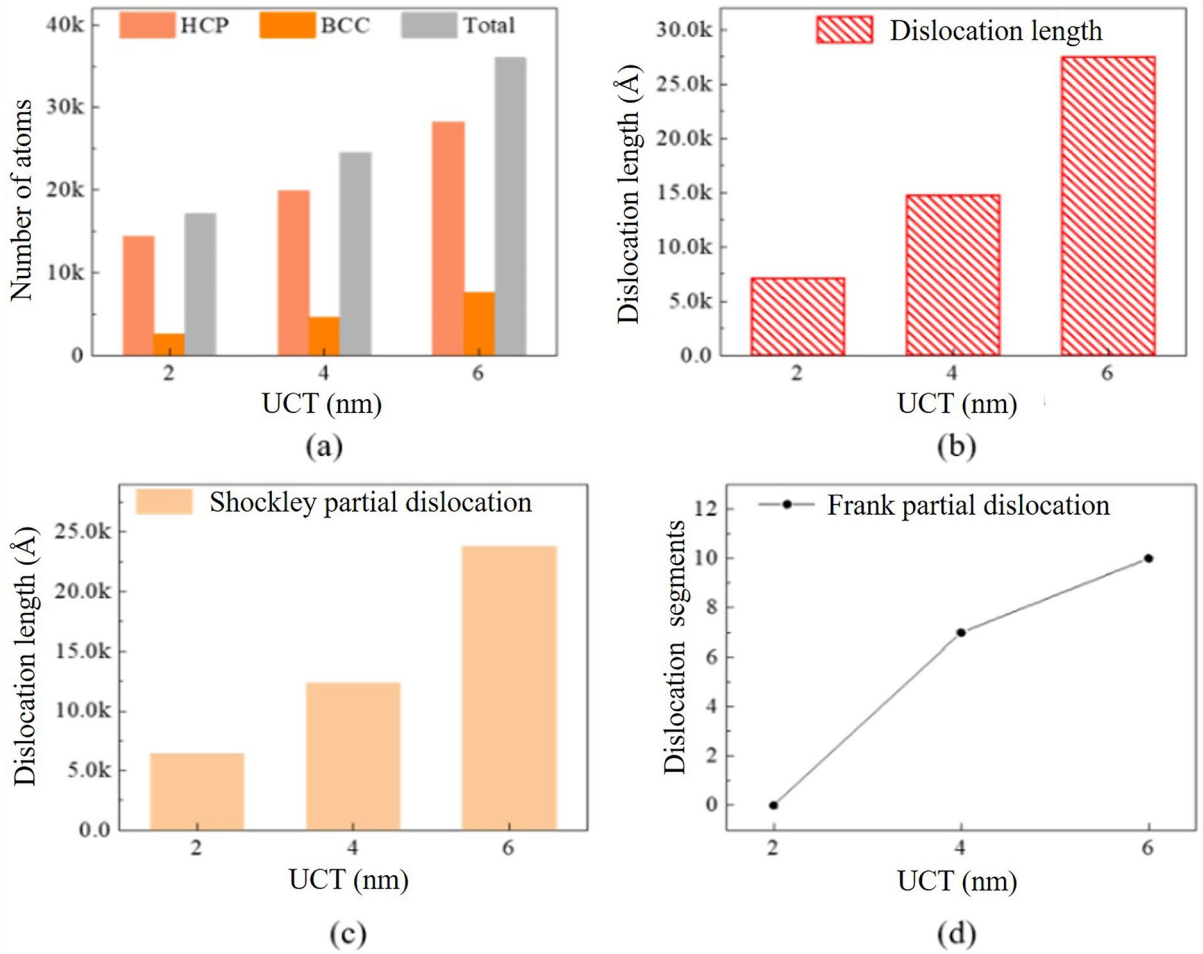

Figure 6 Damage statistics of models with different UCT: (**a**) The number of phase-transition atoms and the total number of changes, (**b**) The total length of dislocation, (**c**) The total length of Shockley partial dislocation, (**d**) The number of Frank partial dislocations

concentrated only below the area of processing. And the phase transition of metallic cerium atoms also occurs during the cutting process. β-Ce is distributed mainly in stacking faults and the coherent twin boundary. In contrast, δ-Ce is only distributed in the processing area. The phase-transition condition of δ-Ce is not reached because the heat generated on the surface of the workpiece is gradually consumed when it is transmitted to the interior of the workpiece.

Figure 8(a) illuminates that when the cutting speed increases, the number of BCC atoms is higher, but the number of HCP atoms decreases first and then increases. This is because when the cutting speed is higher, the workpiece atoms move more violently, which leads to a higher temperature and more δ-Ce phase transition. A comparison of Figure 8(b) and (c) illustrates that the length of the internal dislocation line and Shockley partial dislocation decrease with an increase in cutting speed. The generation of dislocation represents the plastic deformation and the yield of the material. Under the high cutting speed, the strain rate of the material is too high to meet the time required by the proliferation and extension of dislocation, so the plastic deformation of the material is not complete. For the models of low cutting speed, Materials produce a large number of dislocations to meet the requirements of plastic deformation. Figure 8(d) illustrates that the segments of the Frank partial dislocation increase and then decrease significantly with an increase in cutting speed. The maximum and minimum values are 300 m/s and 500 m/s, respectively, proving that the ability of plastic deformation for the workpiece is strong when the cutting speed is 300 m/s. It is proved that when the cutting speed is 300 m/s, there is more dislocation climb inside the workpiece at this time. Consequently, when the cutting speed is 300 m/s, the dislocation intersects are prone to occur, which leads to the dislocation pile-up. This hinders the slippage of Shockley

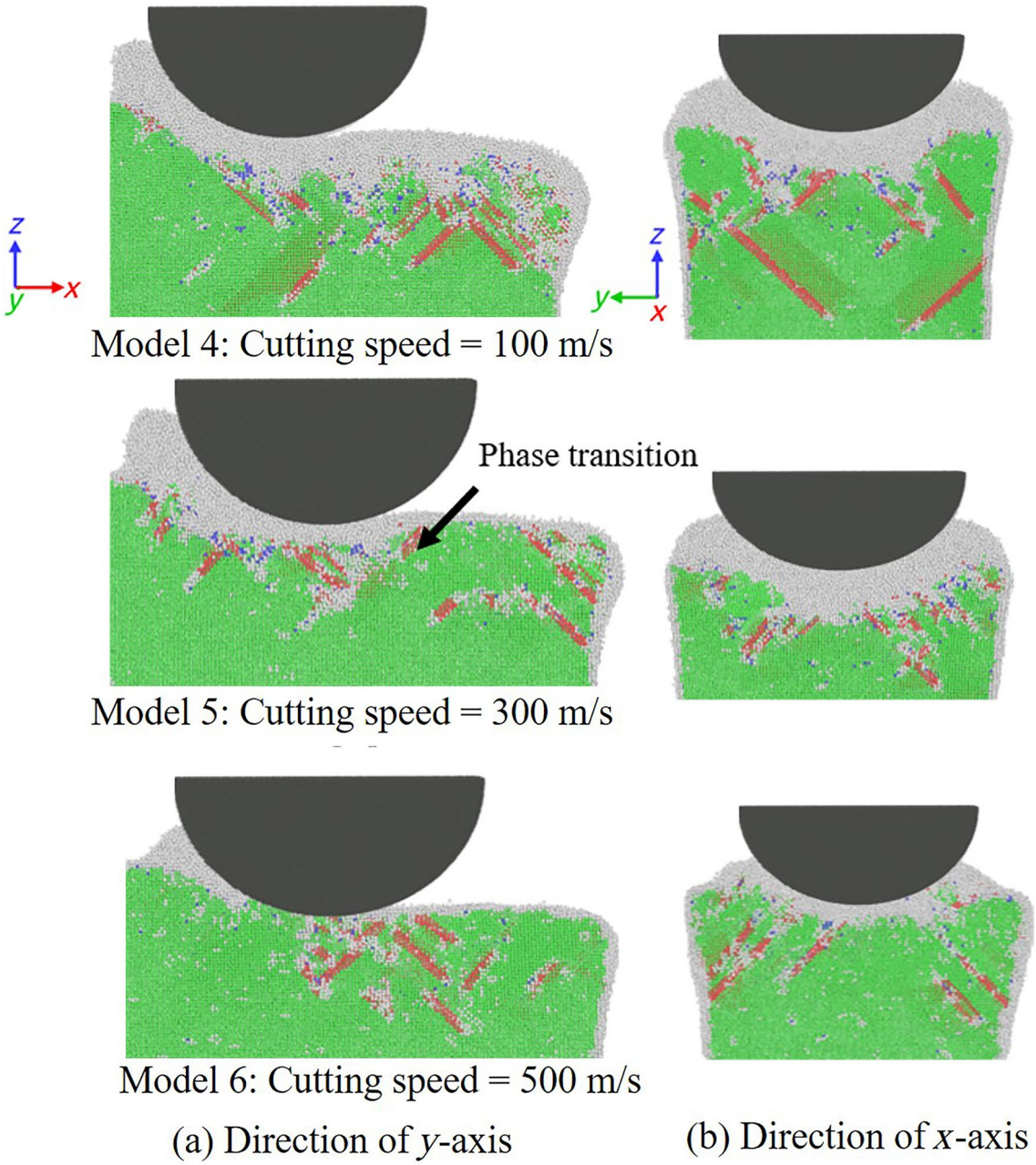

Figure 7 Analysis of subsurface lattice defects of different models: Models 4, 5 and 2 respectively represent the UCT = 4 nm, and the cutting speed = 100 m/s, 300 m/s, 500 m/s: (**a**) Cross section in the direction of *y*-axis, (**b**) Cross section in the direction of *x*-axis

partial dislocation. Compared to the cutting speed is 100 m/s, although the number of Shockley partial dislocations is less, there are enough Frank partial dislocations to activate the mechanism of the dislocation climb inside the workpiece.

In summary, when the cutting speed is lower, the depth of the subsurface defects on the machined surface is deeper and more dislocation and stacking faults are generated. The mechanism of plastic deformation is the slippage of Shockley partial dislocation and the climb of a small amount of Frank partial dislocations. The key to the effect of cutting speed on the plastic deformation ability of cerium–lanthanum alloy is whether there is enough Frank partial dislocation inside the workpiece to activate the mechanism of dislocation climb and dislocation multiplication. Thereby the Shockley partial dislocation

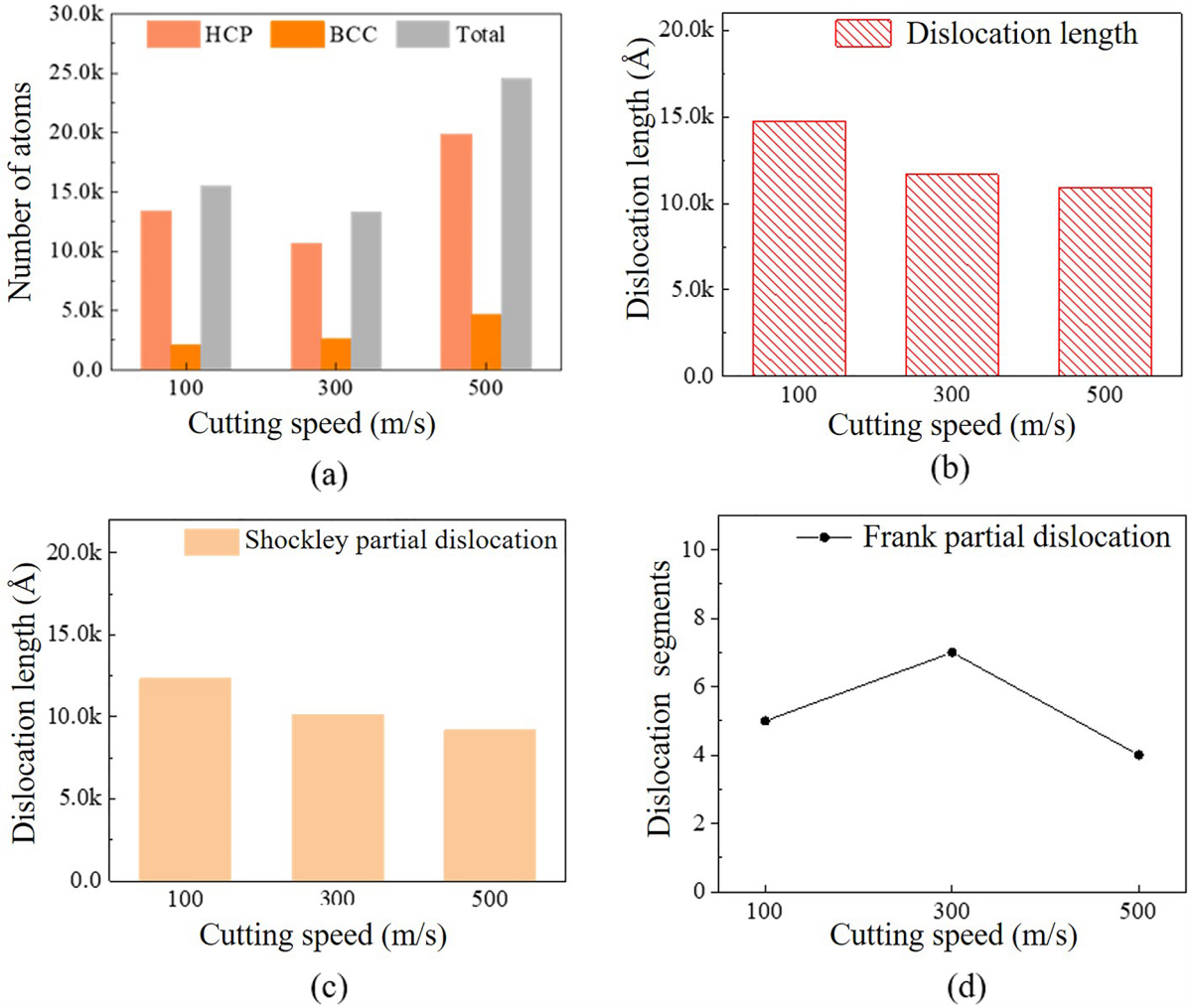

Figure 8 Damage statistics for models with different cutting speeds: (**a**) The number of phase change atoms and the total number of changes, (**b**) The total length of dislocations, (**c**) The total length of Shockley partial dislocations, (**d**) The number of Frank partial dislocations

continues to slip, and the ability of plastic deformation for the cerium–lanthanum alloy is enhanced.

4 Conclusions

MD simulation model was established to study the nanometric cutting mechanism of the cerium–lanthanum alloy. The important details of the nanometric cutting process under different cutting speeds and UCT were analyzed. The main conclusions can be drawn as follows.

(1) The fluctuation of cutting force represents the generation and movement of dislocation subsurface damage for cerium lanthanum alloy. Dislocation nucleated on the cutting surface, which will cause a temporary reduction of cutting force at this moment. When the dislocation pile-up is formed, the external force is needed to increase the work to promote the plastic deformation of cerium–lanthanum alloy. The cutting force will increase at this time.

(2) The phase transitions from γ-Ce to β-Ce occur easily during the nanometric cutting for the cerium–lanthanum alloy. Most of the phase transitions occur in the stacking fault and can extend to the inside of the workpiece. The phase transitions from γ-Ce to δ-Ce occur only in the contact area between the tool and the workpiece because of high pressure and temperature.

(3) The plastic deformation for cerium–lanthanum alloy is mainly due to the glide of Shockley partial dislocation, accompanied by a small amount of the climb of Frank partial dislocation. When the UCT is small, only Shockley partial dislocations glide unevenly on the {1 1 1} plane. Whereas, as the UCT increases, the mechanism of plastic deformation for the cerium–lanthanum alloy becomes the glide of Shockley partial dislocation and the climb of Frank partial dislocation.

(4) The higher the cutting speed, the smaller the depth of the subsurface defects for cerium–lanthanum alloy and the fewer dislocation and stack faults. The most important factor affecting the ability of plastic deformation for the cerium–lanthanum alloy at different cutting speeds is the number of Frank partial dislocations.

Acknowledgements
Not applicable.

Author contributions
CZ conducted the simulation and analyses, and wrote the original manuscript. ML acquired the funding, supervised the research, reviewed and revised the manuscript. FF acquired the funding, supervised and reviewed the manuscript. All authors read and approved the final manuscript.

Authors' Information
Chenyu Zhao, born in 1996, is currently a master candidate at *State Key Laboratory of Precision Measurement Technology and Instruments*, *Laboratory of Micro/Nano Manufacturing Technology (MNMT), Tianjin University, China*.
Min Lai, born in 1987, is an associate professor at *State Key Laboratory of Precision Measurement Technology and Instruments, Laboratory of Micro/Nano Manufacturing Technology (MNMT), Tianjin University, China*. Her research interests include ultra-precision machining and micro/nano manufacturing technology.
Fengzhou Fang, born in 1963, is a professor at *State Key Laboratory of Precision Measurement Technology and Instruments, Laboratory of Micro/Nano Manufacturing Technology (MNMT), Tianjin University, China*, and *Centre of Micro/nano Manufacturing Technology (MNMT-Dublin), University College Dublin, Ireland*. His research interests include ultra-precision manufacturing, optical manufacturing, biological manufacturing and measurement.

Funding
Supported by Science Challenge Project (Grant No. TZ2018006-0201-01) and National Natural Science Foundation of China (Grant Nos. 51605327 and 52035009).

Availability of data and materials
The datasets supporting the conclusions of this article are included within the article.

Declarations

Competing interests
The authors declare no competing financial interests.

Received: 24 March 2022 Revised: 27 July 2023 Accepted: 27 July 2023
Published online: 29 August 2023

References

[1] Y Zhao, W Holzapfel. Structural studies on the phase diagram of cerium. *Journal of Alloys and Compounds*, 1997, 24(6): 216–219. https://doi.org/10.1016/S0925-8388(96)02457-7
[2] K A Gschneidner, V K Pecharsky, J Cho, et al. The β to γ transformation in cerium-A twenty years study. *Scripta Matter,* 1996, 34: 1717–1722. https://doi.org/10.1016/1359-6462(96)00035-8.
[3] D W Wheeler, J Zekonyte, R J K Wood. Mechanical properties of cerium and a cerium-5 wt% lanthanum alloy by nanoindentation and ultrasonic velocity measurements. *Materials Science and Engineering: A*, 2013, 578: 294–302. https://doi.org/10.1016/j.msea.2013.04.083.
[4] J M Crow. 13 elements you can't live without. *New Scientist*, 2011, 210: 36–41. https://doi.org/10.1016/S0262-4079(11)61452-8.
[5] J S Wang, X D Zhang, F Z Fang, et al. A numerical study on the material removal and phase transformation in the nanometric cutting of silicon. *Applied Surface Science*, 2018, 455: 608–615. https://doi.org/10.1016/j.apsusc.2018.05.091.
[6] F Z Fang. Atomic and close-to-atomic scale manufacturing-A trend in manufacturing development. *Frontiers of Mechanical Engineering*, 2016, 11: 325–327. https://doi.org/10.1007/s11465-016-0402-1.
[7] F Z Fang. Atomic and close-to-atomic scale manufacturing: perspectives and measures. *International Journal of Advanced Manufacturing Technology*, 2020, 2: 030201. CNKI:SUN:IJEG.0.2020-03-002.
[8] M Lai, X D Zhang, F Z Fang. Crystal orientation effect on the subsurface deformation of monocrystalline germanium in nanometric cutting. *Nanoscale Research Letters*, 2017, 12: 1–10. https://doi.org/10.1186/s11671-017-2047-3.
[9] Q X Pei, C Lu, F Z Fang, et al. Nanometric cutting of copper: A molecular dynamics study. *Computational Materials Science*, 2005, 37: 434–441. https://doi.org/10.1016/j.commatsci.2005.10.006.
[10] P F Fan, F Ding, X C Luo, et al. A simulated investigation of ductile response of GaAs in single-point diamond turning and experimental validation. *Nanomanufacturing and Metrology*, 2020, 3: 239–250. https://doi.org/10.1007/s41871-020-00080-5.
[11] J J Zhang, H B Zheng, M B Shuai, et al. Molecular dynamics modeling and simulation of diamond cutting of cerium. *Nanoscale Research Letters*, 2017, 12: 1–10. https://doi.org/10.1186/s11671-017-2235-1.
[12] M J Di Wu, X M Hu. Isostructural phase transition of FCC Ce: Molecular dynamics simulations. *Acta Physica Sinica*, 2019, 68: 203401. https://doi.org/10.7498/aps.68.20190884.
[13] J Fu, J J Zhao. Gupta potential for rare earth elements of the FCC phase: lanthanum and cerium. *Modelling and Simulation in Materials Science and Engineering*, 2013, 21: 065003. https://doi.org/10.1088/0965-0393/21/6/065003.
[14] S P Wang, W H Luo, G Li, et al. The effect of lanthanum content on the oxidation kinetics of cerium-lanthanum alloy. *Chemical Research Application*, 2018, 30: 605–609.
[15] J C Wang, J M Zhang, F H Wu, et al. Molecular dynamics modeling and effects of cutting parameters on nanometric cutting process. *Advanced Materials Research*, 2009, 804: 60–61. https://doi.org/10.4028/www.scientific.net/AMR.60-61.435.
[16] H T Liu, X F Zhu, Y Z Sun, et al. Evolution of stacking fault tetrahedral and work hardening effect in copper single crystals. *Applied Surface Science*, 2017, 422: 413–419. https://doi.org/10.1016/j.apsusc.2017.06.059.
[17] J L Abascal, C Vega. A general purpose model for the condensed phases of water: TIP4P/2005. *Journal of Chemical Physics*, 2005, 123: 234505. https://doi.org/10.1063/1.2121687.
[18] A Stukowski. Visualization and analysis of atomistic simulation data with OVITO-the open visualization tool. *Modelling and Simulation in Materials Science and Engineering*, 2010, 18: 015012. https://doi.org/10.1088/0965-0393/18/1/015012.
[19] Y He, M Lai, F Z Fang. A numerical study on nanometric cutting mechanism of lutetium oxide single crystal. *Applied Surface Science*, 2019, 496: 143715. https://doi.org/10.1016/j.apsusc.2019.143715.

[20] C H Chen, M Lai, F Z Fang. Study on the crack formation mechanism in nano-cutting of gallium arsenide. *Applied Surface Science*, 2021, 540: 148332. https://doi.org/10.1016/j.apsusc.2020.148322.
[21] J J Zhang, T Sun, Y D Yan, et al. Molecular dynamics simulation of subsurface deformed layers in AFM-based nanometric cutting process. *Applied Surface Science*, 2008, 254: 4774–4779. https://doi.org/10.1016/j.apsusc.2008.01.096.
[22] C Herbert, D Axinte, M Hardy, et al. Investigation into the characteristics of white layers produced in a nickel-based superalloy from drilling operations. *Procedia Engineering*, 2011, 19: 138–143. https://doi.org/10.1080/10910344.2012.648520.
[23] W Johannes. Elementary dislocation theory, dislocations and imperfections and active centers in semiconductors. *AM. J. Phys*, 1965, 33: 1091–1093. https://doi.org/10.1119/1.1971184